Manipulating the mechanical properties of Ti_2C MXene: Effect of substitutional doping

Poulami Chakraborty,[1] Tilak Das,[2] Dhani Nafday,[1] Lilia Boeri,[3] and Tanusri Saha-Dasgupta[1,*]

[1]*Department of Condensed Matter Physics and Materials Science, S. N. Bose National Center for Basic Sciences, JD Block, Sector III, Salt Lake City, Kolkata 700 106, India*

[2]*Department of Physical Sciences, Indian Institute of Science Education and Research-Kolkata, Mohanpur Campus, PO BCKV Campus Main Office, Nadia 741252, West Bengal, India*

[3]*Institute for Theoretical and Computational Physics, TU Graz, Petersgasse 16, 8010 Graz, Austria*

(Received 31 March 2017; revised manuscript received 26 April 2017; published 18 May 2017)

With the aim of manipulating the mechanical properties of the recently discussed two-dimensional material MXene, we investigate the effect of alloying. We consider substitutional doping of B and V at Ti and C sites of Ti_2C. Calculations of quantities such as in-plane stiffness, Young's modulus, and critical strain through rigorous first-principles technique establish that B doping is highly effective in improving the elastic properties. Oxygen passivation of B-doped Ti_2C in addition to improved elastic properties also exhibits reasonably high critical strains making them ideally suited for applications in flexible devices. Our study further reveals the presence of strong spin-phonon coupling in unpassivated Ti_2C compounds which influences the mechanical behavior. The damage of Ti_2C in its magnetic ground state of A-type antiferromagnetic structure is found to occur at much higher strain than that of the nonmagnetic Ti_2C.

DOI: 10.1103/PhysRevB.95.184106

I. INTRODUCTION

Two-dimensional (2D) solids have generated significant interest and excitement recently. The most prominent example is graphene [1]. Following this excitement, single layers of *h*-BN, MoS_2, and WS_2 have been prepared by micromechanical exfoliation of their three-dimensional (3D) counterparts having van der Waals bonded layered structures [2]. The fascinating properties of these 2D solids have made the research on the discovery and study of novel 2D materials a field of intense activity. Continuing on this effort, a new family of 2D materials has been synthesized very recently by the exfoliation of the layered ternary transition metal carbides, known as MAX phases [3]. The MAX phases represent a large family (≈ 60 compounds) of layered materials of early transition metal carbides and/or nitrides glued together by an A element. The general formula of MAX phases is $M_{n+1}AX_n$ ($n = 1, 2, 3$), where M is usually an early transition metal, A is an A-group element (mostly groups IIIA and IVA), and X denotes carbon or nitrogen. Weaker relative strength of the M-A bonds compared to M-X bonds allows selective etching of the A layer by chemical means without disrupting the M-X bonds. As a consequence the solid is exfoliated into 2D layers. This new 2D family of compounds is termed MXene to denote the removal of A elements from MAX, and to emphasis the structural similarity with graphene [4,5]. Today, the MXene family includes compounds such as Ti_3C_2, Ti_2C, Nb_2C, V_2C, Ti_3CN, and Ta_4C_3 [6]. Since the n values for the existing $M_{n+1}AX_n$ phases can vary from 1 to 3, the corresponding single MXene sheets consist of 3, 5, or 7 atomic layers for M_2X, M_3X_2, and M_4X_3, respectively. In all cases, the individual MXene layer thicknesses are less than 1 nm, while their lateral dimensions can reach tens of microns. MXenes have been discussed as potential candidates for Li-ion battery anodes and as a hydrogen storage medium [7,8].

For practical application of 2D materials, flexibility is an issue to be considered which is related to mechanical properties, i.e., deformability under strain. A few computational studies have been carried out [9–14] focusing on properties of MXene, some specifically focused on elastic properties of $Ti_{n+1}C_n$ [13,14]. These calculations showed 2D Ti_2C to be less stiff compared to graphene or 2D *h*-BN, but stiffer to MoS_2 [13]. It was further shown that surface passivation by termination such as by O improves the mechanical properties in terms of increase in the critical strain value [13]. In this context, it is pertinent to ask, to what extent can the mechanical properties be tailored by solid solutions? Solid solutions in MAX phase have been processed and characterized with substitution on M, A, and X sites, giving rise to compounds such as $(Nb,Zr)_2AlC$, $(Ti,V)_2AlC$, $(Ti,Cr)_2AlC$, $(Ti,Hf)_2InC$, $(Ti,V)_2Sc$, $Ti_3(Si,Ge)C_2$, $Ti_3(Sn,Al)C_2$, $Ti_2Al(C,N)$, and $Ti_3Al(C,N)_2$ [3]. Similarly solid solutions in MXene have been carried out both at M and X sites, giving rise to $(Ti_{0.5}Nb_{0.5})_2C$, $(V_{0.5}Cr_{0.5})_3C_2$, Ti_3CN_x compounds [15], making the option of solid solution compounds a viable one.

In the present study we considered the substitution at both M and X sites of MXene. Considering the specific case of Ti_2C we studied manipulation of the mechanical properties through substitutional doping of B and V at C and Ti sites, respectively. We have considered substitutional doping of Ti_2C with no surface termination as well as oxygen-terminated Ti_2C, i.e., Ti_2CO_2. We carried out calculations of elastic properties such as in-plane stiffness, Young's modulus, Poisson's ratios, and critical strains. B doping is found to significantly improve the elastic properties by reducing the in-plane stiffness and the Young's moduli, as well as extending the yield strength. The origin of the reduction in stiffness is found to be due to weakening of the Ti-B bond compared to the Ti-C bond, reflected in softening of phonon modes. V doping, on the other hand, is found to be much less effective in terms of changing the mechanical properties, causing only a marginal enhancement of in-plane stiffness and Young's modulus. This trend is found to hold good even for B-doped and V-doped

*Corresponding author: t.sahadasgupta@gmail.com

 ©2017 American Physical Society

O-terminated systems. These O-passivated compounds however are found to be materials with relatively high critical strain values compared to their pristine counterparts. Thus B-doped Ti_2CO_2, $Ti_2(C_{0.5},B_{0.5})O_2$, appears to be the best candidate among the studied systems both in terms of reduced stiffness and enhanced critical strain, as compared to pure Ti_2C, thereby showing the promise for improved performance in flexible devices.

While the surface termination leads to nonmagnetic solution of MXene phases, the unpassivated Ti_2C is magnetic. We determined the ground state magnetic structure of pristine Ti_2C which turned out to be antiferromagnetic. Our calculation revealed that the magnetism strongly influences the electronic structure as well as the mechanical properties, due to strong magnetostructural coupling.

II. METHODOLOGY

All DFT calculations on pure and B or V doped Ti_2C or Ti_2CO_2 have been performed using projector augmented wave (PAW) potentials and the plane-wave based Vienna *Ab initio* Simulation Package (VASP) [16]. The exchange-correlation functional was chosen to be that of the generalized gradient approximation (GGA) as implemented in the Perdew-Burke-Ernzerhof (PBE-GGA) formalism [17]. The calculations have been also verified using the local density approximation (LDA). For Ti and V we have used [Ar]$3p3d4s$ configurations as valence configurations while for C, B, and O [He]$2s2p$ configurations were used as valence.

The monolayer of Ti_2C was obtained from the bulk structure of the MAX phase Ti_2AlC by removing the A layer and adding a vacuum of 20 Å along the z direction. The generated quasi-2D monolayer of MXene-structured Ti_2C consists of a hexagonal layer of C atoms sandwiched between top and bottom monoatomic hexagonal Ti planes. 50% of the C (Ti) atoms were replaced by B (V) in order to generate the B-doped (V-doped) Ti_2C compounds. For 50% doping by V and C, a two-formula-unit orthorhombic supercell was considered (shown in the middle panel of Fig. 1), with one out of two Ti atoms belonging to the top layer in the cell being replaced by V, and out of two Ti atoms belonging to the bottom layer in the cell being replaced by V for (Ti,V)C. Similarly for $Ti_2(C_0.5B_0.5)$ one out of two C atoms belonging to the middle layer in the cell is replaced by B. The primitive hexagonal cell of Ti_2C is shown in the left panel of Fig. 1, while the two-formula-unit orthorhombic cell, which is the unit cell for doped compounds, is shown in the middle panel of Fig. 1. Note that the orthorhombic cell has the X direction as the zigzag or nearest-neighbor metal-C(B) bond direction and the Y direction as the armchair or second-nearest-neighbor metal-C(B) bond direction. For our stress-strain calculations, for undoped as well as doped compounds we have considered the two-formula-unit orthorhombic supercell, which allows one to apply the uniaxial strains along the zigzag and armchair direction. The right panel of Fig. 1 shows the Brillouin zone (BZ) of the hexagonal primitive as well as orthorhombic supercell. The structures were fully relaxed to obtain the in-plane lattice parameters and the atomic positions until the Hellmann-Feynman forces became less than 0.001 eV/Å. The structural relaxations were carried out within the non-spin-polarized PAW PBE-GGA+D3 formulation taking into account van der Waals corrections [18]. Subsequent self-consistent electronic structure calculations were carried out on the optimized structures within the spin-polarized GGA approach. In order to check the influence of the missing correlation effect beyond GGA, calculations have been also carried out with supplemented Hubbard U calculations within the GGA+U [19] method with the choice of $U = 4$ eV and $J_H = 0.8$ eV at Ti (V) sites.

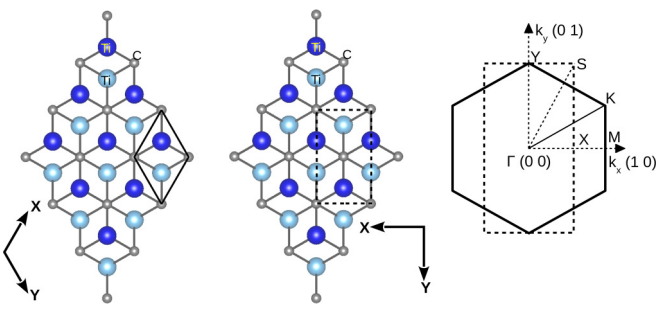

FIG. 1. Left panel: One formula unit, hexagonal primitive cell with three atoms, marked with solid lines in the lattice. The large and small sized balls denote Ti and C atoms, respectively. The Ti atoms belonging to top and bottom layers are colored differently. Middle panel: Two formula units, orthorhombic cell with six atoms, marked with dashed lines in the lattice. Right panel: The primitive cell of the reciprocal lattice corresponding to the hexagonal cell (marked with solid lines) and the orthorhombic cell (marked with dashed lines).

A $12 \times 24 \times 1$ Monkhorst-Pack k-point mesh [20] in the orthorhombic BZ and with an 800 eV plane-wave cutoff was found to provide good convergence of the total energy. The convergence of the energies was ensured using the self-consistency criteria of 10^{-8} eV. In order to cross-check the magnetic ground states in terms of total energy calculations of different chosen magnetic configurations, calculations have been repeated in terms of the all-electron method of the linearized augmented plane wave (LAPW) with no shape approximation to the potential and charge density, as implemented in the Wien2k code [21]. For LAPW calculations, we chose the APW+lo as the basis set and the expansion in spherical harmonics for the radial wave functions was taken up to $l_{max} = 10$. The charge densities and potentials were represented by spherical harmonics up to $l_{max} = 6$. For the number of plane waves, the criterion used was the smallest muffin-tin radius (RMT) multiplied by K_{max} (for the plane wave) yielding a value of 8.0. The RMTs of Ti, V, C, B were chosen to be to 1.15, 1.11, 0.90, 0.95 Å, respectively.

The mechanical properties of 2D MXenes under discussion were studied using the stress-strain relation of the materials upon application of biaxial and uniaxial tensions along zigzag and armchair directions. The strain was applied by increasing both the in-plane lattice parameters for the biaxial case and the lattice parameters along the X or Y axis for uniaxial cases. The structural coordinations were allowed to relax within the PAW PBE-GGA scheme of calculations until the component of the stress tensor along the orthogonal direction due to Hellmann-Feynman forces was below 0.1 GPa. To avoid the influence of the vacuum present in the periodic setup of our calculation, the stress value was scaled by the factor h/d_0, where h is the cell height along the Z axis and d_0 is the thickness of the material.

Phonon calculations have been carried out within the formulation of density functional perturbation theory (DFPT) [22] as implemented in the Quantum Espresso (QE) code [23]. For this purpose, the ground state geometries obtained from VASP were reoptimized within QE using ultrasoft pseudopotentials of Garrity, Bennett, Rabe, and Vanderbilt [24]. The exchange-correlation functional was chosen to be PBE-GGA, as in VASP calculations. The energy cutoffs for the wave function and charge density were set to about 680 eV and 6802 eV, respectively, and the energies were converged to 10^{-10} eV. The ground state geometries and the electronic structure obtained within QE are found to be in good agreement with those obtained with VASP. For phonon calculations, the dynamical matrices were computed on a $4 \times 8 \times 1$ k mesh of the BZ of the orthorhombic cell (cf. Fig. 1), and the phonon band structures, obtained by Fourier interpolation of the real-space force constants, were plotted along the high-symmetry k points of the BZ. In order to have an idea of phonon softening, the frequencies of the phonon modes at the Γ point were computed for 50% B and V doped structures as well as for the pure Ti_2C.

III. RESULTS AND DISCUSSION

In order to study the doping effect on mechanical properties of 2D Ti_2C, we first focus on the electronic and magnetic structures of pristine Ti_2C as well as that of $Ti_2(C_{0.5},B_{0.5})$ and (Ti,V)C. After having an understanding of the underlying electronic and magnetic structures, we present results for elastic properties such as in-plane stiffness, Young's modulus, and Poisson's ratio, followed by the estimate of critical strains. Since the MXene structures synthesized to date [15] are terminated by either O, OH, and/or F, in the final part we consider the doping effect on properties of O-terminated 2D Ti_2C.

A. Electronic and magnetic structures of pristine and doped Ti_2C

The DFT computed non-spin-polarized density of states of Ti_2C shows highly peaked structures at Fermi energy (E_F), with density of states at E_F estimated to be about 4.6 states/eV [25]. Within the Stoner criterion and with a Stoner parameter (I) of Ti as 0.615 [26], this indicates the instability towards ferromagnetism. Indeed the magnetic solution with a parallel alignment of all Ti spins turns out to be lower in energy compared to the nonmagnetic solution by about 100 meV/f.u. with a magnetic moment of $\approx 0.5\ \mu_B$ at each Ti atom. While the magnetism of unpassivated Ti_2C has been reported in the literature [27], to the best of our knowledge, the underlying magnetic structure has not yet been clarified.

In the Ti_2C structure each Ti atom is covalently bonded with three nearest C atoms, while each C atom is bonded with six nearest Ti atoms, three of which belong to the top layer and three belong to the bottom layer. Thus in addition to the ferromagnetic (FM) structure with a parallel alignment of all Ti spins, three different antiferromagnetic (AFM) structures are possible: (i) A-AFM: ferro ordering between intralayer Ti's and antiferro ordering among interlayer Ti's, (ii) C-AFM: antiferro ordering between intralayer Ti's and ferro ordering among interlayer Ti's, and (iii) G-AFM: antiferro ordering between intralayer Ti's and between interlayer Ti's. Total energy calculations for FM, A-AFM, C-AFM, and G-AFM show the A-AFM structure to be lowest in energy, followed by FM structure, while C-AFM and G-AFM structures are found to be lying significantly higher in energy, by more than 100 meV/f.u. The energy difference between the A-AFM and FM structures turned out to be 32 meV/f.u. This suggests the intralayer Ti-Ti coupling to be strongly ferromagnetic, while the interlayer Ti-Ti magnetic interaction to be weaker compared to intralayer coupling and of antiferromagnetic nature. Figure 2 shows the calculated total density of states of Ti_2C in the FM and lowest energy A-AFM magnetic structure. We find that the nearly half-metallic nature of Ti_2C in the FM structure gets destabilized in the A-AFM structure, which becomes semiconducting with an estimated band gap of ≈ 0.2 eV. To the best of our knowledge, the semiconducting nature of bare Ti_2C has not been reported in the literature so far. The inclusion of the correlation effect beyond GGA, through the Hubbard U corrected mean-field theory of GGA+U, is found to keep the qualitative trend unchanged with the A-AFM structure as the lowest energy, though the magnetic moment of individual Ti atoms is found to be enhanced to $\approx 0.7\ \mu_B$. The calculated magnetic moments in GGA and GGA+U have been listed in Table I for the ground state A-AFM structure. The magnetic moments for other magnetic configurations turn out to be rather similar. Since the qualitative trend is found to remain unchanged between GGA and GGA+U calculations, in the following we present results obtained within the GGA scheme of calculation.

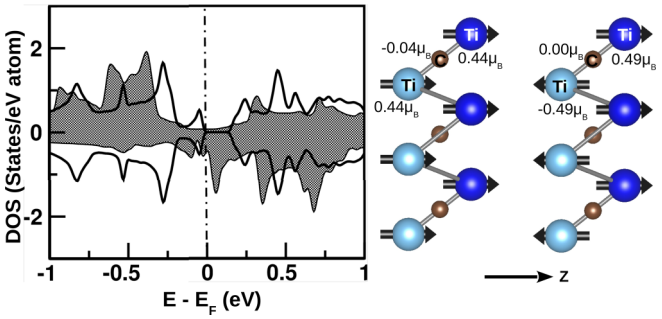

FIG. 2. Left panel: Comparison of calculated density of states corresponding to FM (shaded area) and A-AFM (solid lines) magnetic states plotted as a function of energy. The energy value is measured with respect to GGA Fermi energy, E_F. The alignment and magnitudes of Ti and C moments in FM and A-AFM magnetic configurations are shown in middle and right panels, respectively.

TABLE I. Magnetic moments (in μ_B) at metal (Ti/V) sites in A-AFM phase, calculated within GGA and GGA+U. The moments on C or B are found to be negligibly small.

	GGA			GGA+U		
	TC	TVC	TBC	TC	TVC	TBC
Ti	0.54	0.39	0.48	0.71	0.34	0.74
V		0.47			1.85	

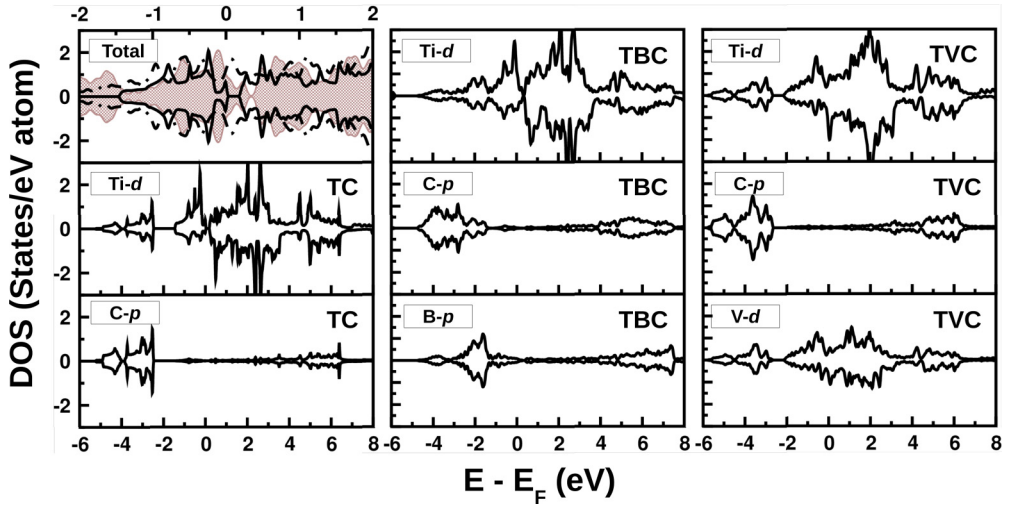

FIG. 3. Total and partial DOS projected to Ti-d, V-d, C-p, and B-p states in Ti_2C (TC), $Ti_2(C_{0.5},B_{0.5})$ (TBC), and (Ti,V)C (TVC) plotted as a function of energy. The comparison of the total DOS of TC (solid lines), TBC (shaded area), and TVC (dashed lines) is shown in the topmost, left column panel, while the plots in other panels show the partial DOS projected either to Ti-d or V-d or C-p or B-p states.

We next consider the effect of substitutional doping at the C site by B, and that at the Ti site by V, by considering $Ti_2(C_{0.5},B_{0.5})$ and (Ti,V)C compounds. We checked the tendency towards segregation versus homogeneous mixing by comparing the energies of the B-rich and C-rich configurations (Ti-rich and V-rich configurations) to that of a uniform mixing of B and C (Ti and V) with alternating arrangement of B and C (Ti and V). The later is found to be energetically stable by about 30–40 meV/f.u. compared to the segregated structure. Introducing B in the structure causes local deformation, with compression in the out-of-plane direction and an in-plane expansion. The reverse is found to be true for substitution of Ti by V. See Fig. S1 in the Supplemental Material [28] for the structural details. Even for the doped compounds the A-AFM magnetic structure is found to be the lowest energy magnetic configuration followed by FM structure while the energies for G-AFM and C-AFM magnetic structures turn out much higher, following the same trend as the undoped Ti_2C. The energy difference between A-AFM and FM structure turned out to be ≈ 10 meV/f.u. for $Ti_2(C_{0.5},B_{0.5})$, and ≈ 100 meV/f.u. for (Ti,V)C. Thus while the B doping somewhat weakens the interlayer magnetic coupling, V doping enhances it substantially.

Figure 3 shows the plot of the density of states (DOS) for Ti_2C, $Ti_2(C_{0.5},B_{0.5})$, and (Ti,V)C compounds for the lowest energy A-AFM magnetic structure. Note B substitution at the C site causes hole doping, while V substitution at the Ti site causes electron doping in the system. This together with local deformation makes the system metallic as seen from the plot in the left, topmost panel in Fig. 3. As is evident from the plots of partial density of states, presented in the remaining panels of Fig. 3, for Ti_2C, the Ti-d-C-p hybridized bonding states appear in the energy range about -5.0 eV to about -2.5 eV, separated by a gap of ≈ 1.0 eV from the nonbonding Ti-d dominated states spanning an energy range of ≈ -1.5 eV to $\approx +4$ eV, and arising out of metal-metal bonding. The higher lying states from ≈ 4 eV to 6 eV are contributed by Ti-d-C-p hybridized antibonding states. The Ti-d-B-p hybridized bonding states for $Ti_2(C_{0.5},B_{0.5})$ appear in the energy range ≈ -3 eV to ≈ -0.5 eV, shifted with respect to Ti-d-C-p hybridized bonding states, signaling the difference in the strength of hybridization between C-p and B-p with Ti-d. This in turn closes the energy gap between nonbonding and bonding states in the case of $Ti_2(C_{0.5},B_{0.5})$ which was observed for Ti_2C. In the case of (Ti,V)C, the gap between the nonbonding and bonding states persist with nonbonding V-d dominated states spanning almost the same energy range as that of Ti-d dominated nonbonding states.

B. Mechanical properties of pristine and doped Ti_2C

We have studied the mechanical response of the pristine and doped Ti_2C under three different loading conditions of the tensile strain: biaxial tension and uniaxial tensions along the X and Y directions of the orthorhombic cell. We applied a series of incremental tensile strains in the cell, and, as mentioned already, simultaneously relaxed the other stress components to zero which takes into account Poisson contraction under uniaxial tension. In the following we first discuss the elastic properties, and then the critical strains.

1. Stress-strain relations: Elastic properties

The calculated stress-strain curves for pristine Ti_2C are shown in Fig. 4. The left panel of the figure shows the result for nonmagnetic (NM) Ti_2C, while the right panels show the comparison of the stress-strain curves between the nonmagnetic Ti_2C and Ti_2C in the lowest energy magnetic state of A-AFM. The elastic constants can be extracted by linear fit to the stress-strain curves for small strain values. We note that unlike graphene or h-BN, Ti_2C is a two-dimensional multiplanar hexagonal structure, and therefore quasi-2D. As discussed in Ref. [29] from a structural point of view the general 2D materials can be classified into four different classes. According to that general classification, the MXene family of compounds such as Ti_2C belongs to class D, where the constituent atoms are not the same and they belong

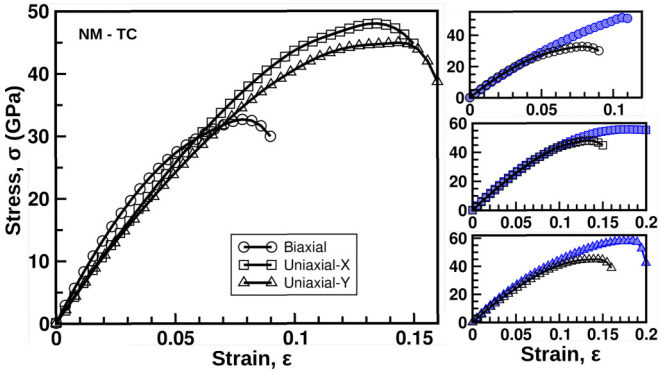

FIG. 4. The stress-strain curve of the pristine Ti_2C under biaxial and uniaxial tensile strains along the zigzag (uniaxial-X) and armchair (uniaxial-Y) directions. The left panel shows the results for NM state of Ti_2C. The top, middle, and bottom right panels show the comparison for NM (open symbols) and A-AFM (shaded symbols) states under biaxial, uniaxial-X, and uniaxial-Y loading of strain.

to different planes. Even though these structures have a hexagonal top view, different atoms are found to be placed in different planes. The high-fidelity analytical model developed in Ref. [29] starting from equivalent elastic properties of atomic bonds shows that the elastic properties of quasi-2D materials belonging to class D needs to be described by two Young's moduli (E_1 and E_2) and two Poisson's ratios (ν_{12} and ν_{21}), 1 and 2 directions referring to zigzag and armchair directions. Graphene or h-BN belonging to class A or class B, on the other hand, can be described by a single Young's modulus and a single Poisson's ratio with $E_1 = E_2$, and $\nu_{12} = \nu_{21}$. Our DFT calculations show that for our studied systems E_1 and E_2 differ by 3%–4% with $E_1 > E_2$, in agreement with findings of a previous DFT study [13]. This suggests that the Ti_2C family of compounds is nearly isotropic, as opposed dichalcogenides such as MoS_2 [29]. For the ease of comparison between different 2D materials we have quoted $E = (E_1 + E_2/2)$. Similarly, our calculations show that for our studied systems ν_{12} and ν_{21} differ by 3%–5%. As in the case of Young's modulus, we have quoted $\nu = (\nu_{12} + \nu_{21})/2$.

In the case of 2D materials, because of the reduced dimensionality of these materials, it makes more sense to define the in-plane stiffness, C, which is nothing but E^{2D} instead of the classical 3D Youngs modulus, as extensively used in literature for different 2D materials [13,30]. This can be obtained by fitting the initial slope of the stress-strain curve under the condition of biaxial strain. The calculated in-plane stiffness, Young's modulus (E), and Poisson's ratio (ν) are listed in Table II. Comparing the stress-strain curves between the NM state and A-AFM state, as presented in the right column of the figure, we find that while the effect of magnetism is relatively small in the linear regime or the harmonic region of the strain, it has significant influence in the nonlinear or the anharmonic region. The damage of the A-AFM phase occurs at higher strain than that of the NM phase. This indicates the presence of rather strong magnetostructural coupling, which we will come back to in the following.

Comparison of stress-strain curves between pristine and B/V-doped Ti_2C is presented in Fig. 5. Focusing on the linear

TABLE II. Elastic constants of pure Ti_2C and B-doped and V-doped compounds. For comparison, the previously calculated elastic constants of pure Ti_2C [13], MoS_2 [31], graphene [31], h-BN [32], and SiC [32] are also listed. The in-plane stiffness constant (C) and Young moduli (E) are in GPa, while the biaxial and uniaxial critical strain values are given in %. To compare with elastic constant values of other 2D materials, as given in Refs. [31,32], our calculated in-plane stiffness constants are also quoted in N/m in parentheses.

				Critical Strain			
		C	E	ε_{c1}^{bi}	ε_{c1}^{1}	ε_{c1}^{2}	ν
TC	NM	704 (142)	577	8	13	14	0.366
	AFM	715 (152)	586	11	18	18	0.292
TVC	NM	738 (152)	590	6	14	15	0.399
	AFM	742 (157)	596	4	11	11	0.360
TBC	NM	515 (120)	426	5	11	11	0.365
	AFM	521 (124)	432	10	16	14	0.301
Pure Ti_2C	Ref. [13]		610	9.5	18	17	
MoS_2	Ref. [31]	120.1					0.254
Graphene	Ref. [31]	340.8					0.178
h-BN	Ref. [32]	275.8					0.220
SiC	Ref. [32]	163.5					0.300

regime a significant difference is found between the elastic properties of Ti_2C and $Ti_2(C_{0.5},B_{0.5})$. Extracted values of in-plane stiffness, Young's modulus, and for Poisson's ratio for $Ti_2(C_{0.5},B_{0.5})$ and (Ti,V)C are listed in Table II for the NM state as well as for the A-AFM state. There is about 25%–27% decrease in in-plane stiffness as well as in Young's modulus of $Ti_2(C_{0.5},B_{0.5})$ compared to that of the Ti_2C. Substitutional doping of V at the Ti site, on the other hand, is found to keep the stiffness similar to the undoped Ti_2C. The computed elastic properties of other 2D materials, as reported in literature, are also listed in Table II. On comparison, we find that undoped Ti_2C is much less stiff compared to graphene or h-BN, though somewhat stiffer compared to MoS_2, as discussed before. B doping helps in reducing the in-plane stiffness, bringing it down to the level of MoS_2.

The appreciable reduction in elastic properties under substitutional B doping can be rationalized by the weakening of the Ti-B bond as compared to the Ti-C bond. Figure 6 shows the plot of the charge density which highlights the relatively stronger covalency between Ti and C compared to that between Ti and B. This is further corroborated by the calculated phonon frequencies at the Γ point (cf. Fig. 7). Upon B doping, the low-frequency phonon modes are found to shift to the lower frequencies to a large extent, while only marginal shifts are observed for V doping. The modes associated with such low-frequency modes, as shown in the insets, correspond to atomic displacements related to movement of Ti-C, Ti-B, or V-C bonds. Since the phonon frequency (ω) is related to the bond stiffness (κ) as $\omega \propto \sqrt{\kappa}$, the softening of these modes confirms the weakening of Ti-B bonds compared to Ti-C bonds, as concluded from charge-density plots.

2. *Critical strains*

As mentioned above, the stress-strain curve is characterized by a linear or harmonic region at small strain values, followed

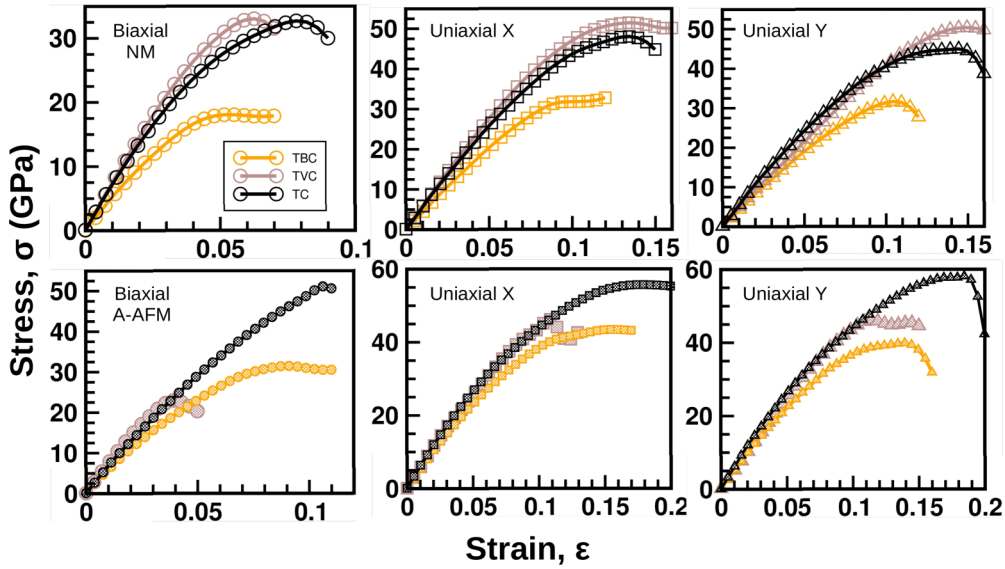

FIG. 5. The stress-strain curve of Ti_2C, $Ti_2(C_{0.5},B_{0.5})$, and (Ti,V)C under biaxial and uniaxial tensile strains along the X and Y directions. The top panels show the results for NM states, while the bottom panels show the results for the minimum energy A-AFM magnetic state.

by an anharmonic region where higher-order terms in strain energy start to become important. The nonlinear mechanical property is anisotropic [33,34], thereby giving rise to different critical strain values in biaxial and different uniaxial tensions, applied along the zigzag and armchair directions of the orthorhombic supercell. Following the stress-strain plots, the critical strain value, ϵ_{c1}, is characterized by the strain value at which the stress attains its maximum value after which the stress starts to fall and instability sets in. This provides a measure of the highest withstanding of the strain. Table II lists the values of ε_{c1} for Ti_2C, $Ti_2(C_{0.5},B_{0.5})$, and (Ti,V)C under biaxial and uniaxial strains in the X and Y directions, referred to as ε_{c1}^{bi}, ε_{c1}^{1}, and ε_{c1}^{2}, respectively. As is seen, magnetism has a strong influence in the values of ϵ_{c1}, increasing it from 8%, 13%, and 14% to 11%, 18%, and 18% for Ti_2C under biaxial, uniaxial-X, and uniaxial-Y tensile strains. A similar trend is generally observed for $Ti_2(C_{0.5},B_{0.5})$, though a slight decrease has been observed for (Ti,V)C under biaxial strain.

Figure 8 shows the phonon dispersion plotted along the high-symmetry points of the orthorhombic BZ for Ti_2C in NM and A-AFM ordered phase. As is evident from the plot, inclusion of magnetism changes the phonon frequencies significantly hinting towards the presence of strong spin-phonon coupling. We find, in general, dispersions to be stiffer for AFM Ti_2C compared to NM Ti_2C, especially at the vicinity of the Γ point. Given the fact that the slopes of the dispersion curves close to Γ can be expressed as the square root of the elastic constant (or combinations) over density, this amounts to increased stiffness of the Ti_2C in the AFM phase compared to NM. This is supported by the calculated elastic constants (cf. Table II). The three lowest energy branches designate three acoustic (A) branches corresponding to long-wavelength vibrations, classified as LA, TA, and ZA (cf. Fig. 8), where L stands for longitudinal polarization, T for in-plane transverse polarization, and Z for out-of-plane transverse polarization. For NM Ti_2C, the ZA branch close to Γ shows the quadratic dispersion, which is a characteristic feature of other 2D materials as well, such as graphene [35]. This very soft mode, which propagates parallel to the layer, corresponds to the

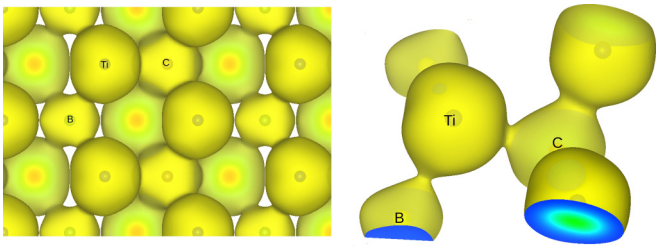

FIG. 6. The plot of calculated charge density for $Ti_2(C_{0.5},B_{0.5})$. The isosurface value is chosen at 0.065 $e^-/Å^3$. Left panel shows the plot in an extended region, while the right panel presents zoomed view focused on central Ti atom bonded with B and C. The stronger covalency of the Ti-C bond compared to the Ti-B bond is visible.

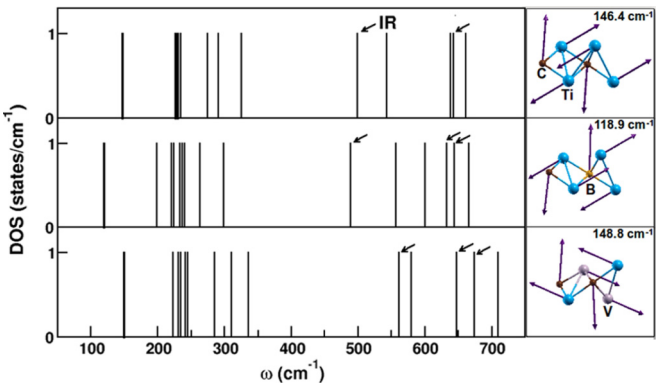

FIG. 7. Calculated optical phonon (Γ point) frequencies for Ti_2C (top panel), $Ti_2(C_{0.5},B_{0.5})$ (middle panel), and (Ti,V)C (bottom panel). The arrows highlight the infrared (IR) active modes. The insets in the right column show the atomic displacements corresponding to lowest frequency modes in each case.

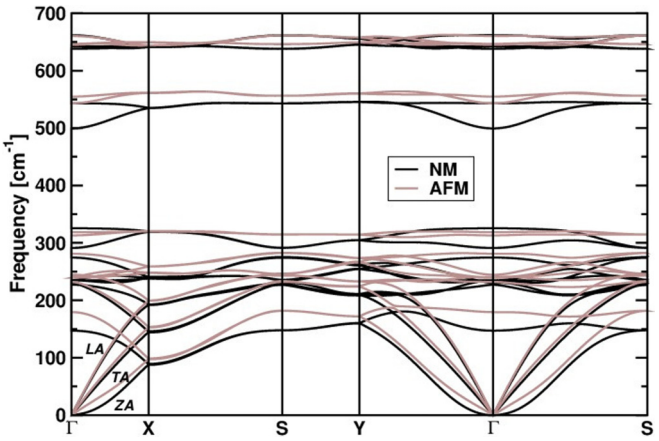

FIG. 8. Phonon dispersion of Ti_2C in the NM and ground state magnetic structure of A-AFM.

layer-bending or *ripple* mode [36]. In AFM Ti_2C the dispersion corresponding to ZA modes changes considerably compared to NM Ti_2C suggestive of hardening of such layer-bending or ripple mode. This justifies the observation that AFM Ti_2C can withstand significantly higher strain as compared to NM Ti_2C (cf. Fig. 4 and discussions therein).

The anharmonic region is followed by a plastic region where irreversible structural changes occur in the system and it transforms into a different structure after the yielding point. The second critical point, ϵ_{c2}, is the yielding point and marks the boundary between elastic and plastic regions. Up to ϵ_{c2}, the system preserves the hexagonal symmetry and upon release of strain the system reverts back to the unstrained structure. We have estimated ϵ_{c2} for the biaxial strain. For this purpose, we plotted the strain energy (E_s) as a function of biaxial strain (ϵ). The strain energy is calculated by subtracting the total energy of the strained system from the equilibrium total energy, and related to stress, as $\sigma = \frac{dE_s}{d\epsilon}$. The E_s versus ϵ plot for NM Ti_2C is shown in the left panel of Fig. 9. ϵ_{c2} is given by the strain value at which the strain energy drops, which in the present case is estimated to be 27%. The structure at this strain value is shown in the right panel of Fig. 9, which demonstrates the deviation of the structure from the hexagonal

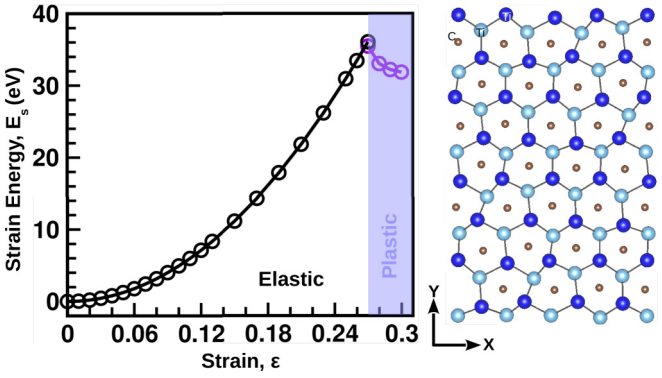

FIG. 9. Left panel: The variation of strain energy as a function of the biaxial strain for Ti_2C. The strain value at which the drop in the strain energy occurs denotes the second critical point, ϵ_{c2}. Right panel: The structure of Ti_2C at the strain value of ϵ_{c2}.

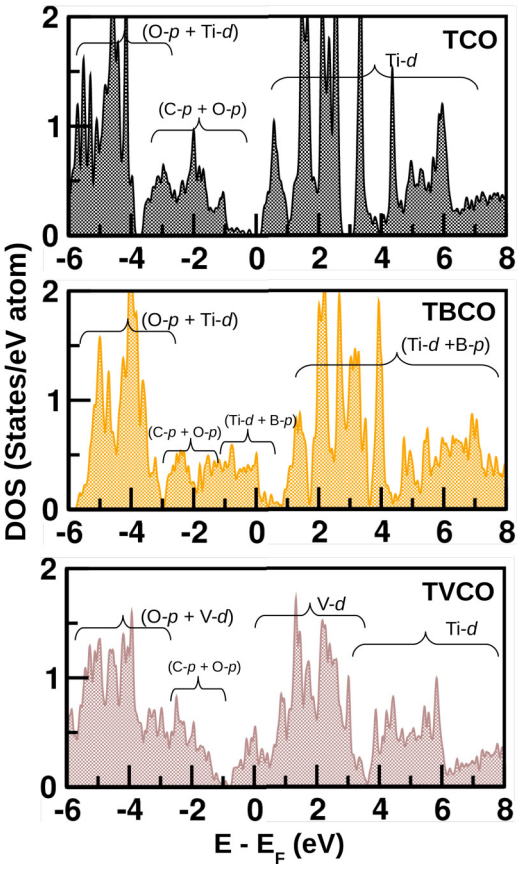

FIG. 10. The density of states for O-passivated Ti_2C (TCO) (top panel), B-doped Ti_2C (TBCO) (middle panel), and V-doped Ti_2C (TVCO) (bottom panel) plotted as a function of energy. The dominant orbital characters have been marked.

symmetry at the yield point. We note that the presence of defects and the temperature effect can reduce our estimated ϵ_{c2} value significantly. Repeating the same exercise for B-doped Ti_2C, the value of ϵ_{c2} was estimated to be $\approx 33\%$ indicating effectiveness of B doping in also enhancing the yield strength. V doping, on the other hand, is found to reduce the ϵ_{c2} value slightly with an estimated value of 26%. Introduction of magnetism does not appear to have significant influence on ϵ_{c2} values.

C. Effect of O termination on mechanical properties

Finally we consider the effect of termination by O. Three possible configurations of termination exist [27]: (i) configuration I: O's are located above the hollow site of three neighboring C/B atoms and point to the Ti/V atoms in the second Ti/V layer on both sides of MXene, (ii) configuration II: O's are located above the C/B atoms for both sides of MXene, (iii) configuration III: configuration I on one side and configuration II on the opposite side. Our total energy calculations show configuration I to be the minimum energy configuration among the three in conformity with previous findings [27]. In the following, we thus considered only configuration I as far as termination is concerned. The created local strain due to substitutional doping of B at the C site and V at the Ti site makes the average thickness of the O-passivated

TABLE III. Elastic properties for pure Ti_2CO_2 (TCO) and B-doped (TBCO) and V-doped (TVCO) cases. The in-plane stiffness constant (C) and Young's modulus (E) are in GPa while the critical strain value (ϵ_{c1}) is given in %. The DFT calculated elastic constants for TCO as given in Ref. [13] are also listed.

			Critical Strain			
	C	E	ε_{c1}^{bi}	ε_{c1}^{1}	ε_{c1}^{2}	ν
TCO	745	570	23	28	26	0.303
TCO [13]		567	20	28	26.5	
TVCO	794	560	22	9	28	0.340
TBCO	587	431	16	15	25	0.360

MXene larger by about 2% in the doped cases compared to the undoped Ti_2CO_2. For the details of the structures see the Supplemental Material [28].

We find that O termination leads to complete quenching of magnetism in Ti_2C, as reported already [37], as well as in $Ti_2(C_{0.5},B_{0.5})$ and (Ti,V)C. Figure 10 shows the calculated density of states for Ti_2CO_2, $Ti_2(C_{0.5},B_{0.5})O_2$, and $(Ti,V)CO_2$. We find that O-passivated Ti_2C is semiconducting, as reported earlier [27]. Hole (electron) doping by B (V) makes the system metallic. The states lying low far from E_F are primarily Ti-d-(V-d-)O-p, Ti-d-B-p, or Ti-d-(V-d-)C-p bonding states, while the dominant states close to E_F are Ti-d (V-d) non-bonding states. The high lying states away from E_F are the antibonding states arising out of Ti-d-(V-d-)O-p, Ti-d-B-p, or Ti-d-(V-d-)C-p hybridization.

The stress-strain curves for Ti_2CO_2, $Ti_2(C_{0.5},B_{0.5})O_2$, and $(Ti,V)CO_2$ under biaxial, uniaxial-X, and uniaxial-Y tensile strains are plotted in Fig. 11. We find the change in slope of the linear regime in the B-doped compounds compared to that of the undoped or V-doped compounds, similar to that observed for the unpassivated compounds. The computed in-plane stiffness, Young's modulus, critical strain, ϵ_{c1}, for undoped and doped compounds are tabulated in Table III. There are a few observations to be made. First of all, we observe a general increase in the ϵ_{c1} value in the O-passivated compounds compared to unpassivated compounds. For undoped Ti_2C, this increase is 45% to 100% in agreement with previous literature [13]. For B and V doped compounds, this trend is maintained except for uniaxial X for which a decrease is observed. For B-doped Ti_2C the increase in ϵ_{c1} for biaxial and uniaxial Y for O-terminated compound is about 60%−80% compared to unpassivated compounds, while for V-doped Ti_2C this increase is very large, being 1.5 to 4.5 times. The second important observation is that the trend of suppression of stiffness as well as that of Young's modulus in B-doped compounds compared to the undoped compound continues to be the case even for passivated compounds. The suppression of in-plane stiffness and Young's modulus is found to be 21%−26%, rather similar to that found for the unpassivated compounds.

IV. CONCLUSIONS

The newest addition to the list of 2D materials with fascinating properties is MXene compounds, which are 2D counterparts of 3D hexagonal MAX compounds. To make these materials commercially useful, an important issue is the improvement of properties. Among the various possible routes to do so, one is alloying with other elements. In the present study we focus on the mechanical properties and study the effect of alloying at both X and M sites of MXene. In particular, we take up the representative case of Ti_2C and consider the solid solutions $Ti_2(C_{0.5},B_{0.5})$ and (Ti,V)C. Since the Ti_2C compounds synthesized so far are all reported to be passivated, we also consider the effect of O passivation. Our study concludes that B doping of O-passivated Ti_2C compound makes it a system with improved mechanical properties both in terms of reduced stiffness (by about 27%) and extended critical strain (by about 100%) compared to the pristine unpassivated Ti_2C compound. The microscopic origin of the improved elastic properties upon B doping has been traced to the weakening in the covalency of the Ti-B bond compared to that of the Ti-C bond, a fact also supported by phonon calculations.

Our study additionally reports an interesting observation in terms of magnetism of unpassivated Ti_2C, which to the best of our knowledge has remained unexplored so far. We clarify the magnetic ground state to be of A-AFM type having the Ti spins between the top and bottom layers aligned in an antiparallel manner. The stabilization of A-AFM structure drives the semiconducting behavior of Ti_2C as compared to previously reported metallic or half-metallic behavior of Ti_2C [25,38]. Interestingly we find that AFM order hardens the phonon frequencies having the significant influence on the out-of-plane layer-bending or rippling mode. This makes unpassivated Ti_2C in its ground state A-AFM structure withstand larger strain compared to that of NM Ti_2C. This in turn highlights the significant role of spin-phonon coupling in magnetic MXene materials, a topic which needs to be explored in the future.

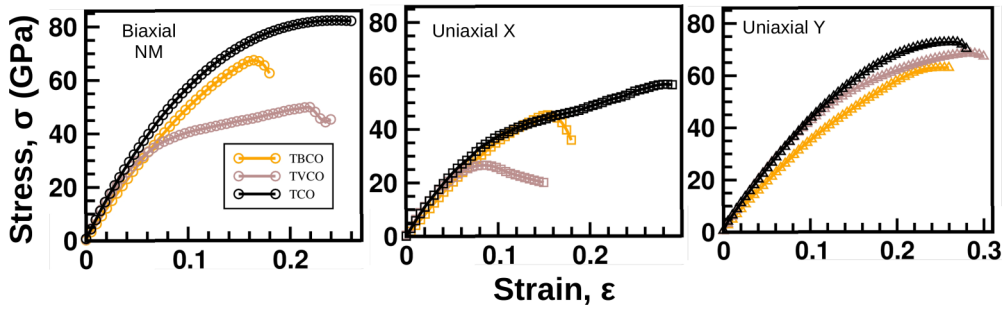

FIG. 11. The stress-strain curve of Ti_2CO_2, $Ti_2(C_{0.5},B_{0.5})O_2$, and $(Ti,V)CO_2$ under biaxial and uniaxial tensile strains along the X and Y directions.

ACKNOWLEDGMENTS

The authors thank the Department of Science and Technology, India, for support through the Thematic Unit of Excellence. T.S.-D. and L.B. thank the Indo-Austrian bilateral project for collaboration.

[1] K. S. Novoselov, A. K. Geim, S. V. Morozov, D. Jiang, Y. Zhang, S. V. Dubonos, I. V. Gregorieva, and A. A. Firsov, Science **306**, 666 (2004); Y. Zhang, Y. W. Tan, H. L. Stormer, and P. Kim, Nature (London) **438**, 201 (2005); A. K. Geim and S. K. Novoselov, Nat. Mater. **6**, 183 (2007).

[2] A. Gupta, T. Sakthivel, and S. Seal, Prog. Mater. Sci. **73**, 44 (2015).

[3] M. Radovic and M. W. Barsoum, Am. Ceram. Soc. Bull. **92**, 20 (2013).

[4] M. Naguib, V. N. Mochalin, M. W. Barsoum, and Y. Gogotsi, Adv. Mater. **26**, 992 (2014).

[5] Z. Guo, L. Zhu, J. Zhou, and Z. Sun, RSC Adv. **5**, 25403 (2015).

[6] M. Naguib, O. Mashtalir, J. Carle, V. Presser, J. Lu, L. Hultman, Y. Gogotsi, and M. W. Barsoum, ACS Nano **6**, 1322 (2012).

[7] Q. Tang, Z. Zhou, and P. Shen, J. Am. Chem. Soc. **134**, 16909 (2012).

[8] Q. Hu, D. Sun, Q. Wu, H. Wang, L. Wang, B. Liu, A. Zhou, and J. He, J. Phys. Chem. A **117**, 14253 (2013).

[9] I. R. Shein and A. L. Ivanovskii, Comput. Mater. Sci. **65**, 104 (2012).

[10] S. Zhao, W. Kang, and J. Xue, Appl. Phys. Lett. **104**, 133106 (2014).

[11] M. Khazaei, M. Arai, T. Sasaki, C.-Y. Chung, N. S. Venkataramanan, M. Estili, Y. Sakka, and Y. Kawazoe, Adv. Funct. Mater. **23**, 2185 (2013).

[12] H. Lashgari, M. R. Abolhassani, A. Boochani, S. M. Elahi, and J. Khodadadi, Solid State Commun. **195**, 61 (2014).

[13] Z. Guo, J. Zhou, C. Si, and Z. Sun, Phys. Chem. Chem. Phys. **17**, 15348 (2015).

[14] M. Kurtoglu, M. Naguib, Y. Gogotsi, and M. W. Barsoum, MRS Commun. **2**, 133 (2012).

[15] M. Naguib, M. Kurtoglu, V. Presser, and M. Barsoum, Adv. Mater. **23**, 4248 (2011).

[16] G. Kresse and J. Hafner, Phys. Rev. B **47**, 558(R) (1993); G. Kresse and J. Furthmüller, *ibid.* **54**, 11169 (1996).

[17] J. P. Perdew, K. Burke, and M. Ernzerhof, Phys. Rev. Lett. **77**, 3865 (1996).

[18] S. Grimme, J. Antony, S. Ehrlich, and S. Krieg, J. Chem. Phys. **132**, 154104 (2010).

[19] V. I. Anisimov, I. V. Solovyev, M. A. Korotin, M. T. Czyżyk, and G. A. Sawatzky, Phys. Rev. B **48**, 16929 (1993).

[20] H. J. Monkhorst and J. D. Pack, Phys. Rev. B **13**, 5188 (1976).

[21] P. Blaha, K. Schwarz, G. K. H. Masden, D. Kvasnicka, and J. Luitz, in *Wien2k, An Augumented Plane Wave + Local Orbitals Program for Calculating Crystal Properties*, edited by K. Schwarz (Technische Universitiät Wien, Vienna, 2001).

[22] S. Baroni, P. Giannozzi, and A. Testa, Phys. Rev. Lett. **58**, 1861 (1987).

[23] P. Giannozzi, S. Baroni *et al.*, J. Phys.: Condens. Matter **21**, 395502 (2009).

[24] K. F. Garrity, J. W. Bennett, K. M. Rabe, and D. Vanderbilt, Comput. Mater. Sci. **81**, 446 (2014).

[25] S. Wang, J. Li, Y. Du, and C. Cui, Comput. Mater. Sci. **83**, 290 (2014).

[26] C.-M. Fang, R. S. Koster, W.-F. Li, and M. A. van Huis, RSC Adv. **4**, 7885 (2014).

[27] Y. Xie and P. R. C. Kent, Phys. Rev. B **87**, 235441 (2013).

[28] See Supplemental Material at http://link.aps.org/supplemental/10.1103/PhysRevB.95.184106 for structural details of the pristine, B-doped, and V-doped Ti_2C and Ti_2CO_2.

[29] T. Mukhopadhyay, A. Mahata, S. Adhikari, and M. Asle Zaeem, 2D Mater. **4**, 025006 (2017).

[30] M. Topsakal, S. Cahangirov, and S. Ciraci, Appl. Phys. Lett. **96**, 091912 (2010).

[31] Q. Peng and S. De, Phys. Chem. Chem. Phys. **15**, 19427 (2013).

[32] R. C. Andrew, R. E. Mapasha, A. M. Ukpong, and N. Chetty, Phys. Rev. B **85**, 125428 (2012).

[33] L. Colombo *et al.*, Rep. Prog. Phys. **74**, 116501 (2011).

[34] J. F. Nye, *Physical Properties of Crystals* (Clarendon, Oxford, 1985).

[35] N. Mounet and N. Marzari, Phys. Rev. B **71**, 205214 (2005).

[36] H. Zabel, J Phys: Condens. Matter **13**, 7679 (2001).

[37] H. Zhang, G. Yang, X. Zuo, H. Tang, Q. Yang, and G. Li, J. Mater. Chem. A **4**, 12913 (2016).

[38] G. Gao, G. Ding, J. Li, K. Yao, M. Wu, and M. Qian, Nanoscale **8**, 8986 (2016).